

17. R. J. Veitch, *Phys. Earth Planet. Inter.* **23**, 215 (1980); R. J. Veitch and A. Stephenson, *ibid.* **16**, 209 (1978).
18. D. J. Dunlop, *ibid.* **26**, 1 (1981), p. 5; D. J. Dunlop, *J. Geophys. Res.* **81**, 3511 (1976).
19. H. P. Johnson and R. T. Merrill, *J. Geophys. Res.* **79**, 5533 (1974); F. Heider and D. J. Dunlop, *Phys. Earth Planet. Inter.* **46**, 24 (1987).
20. W. P. Osmond, *Proc. Phys. Soc. London* **B66**, 265 (1953); D. H. Lindsley, in *Oxide Minerals*, vol. 3 of *Reviews of Mineralogy*, D. Rumble III, Ed. (Mineralogical Society of America, Washington, DC, 1976), p. L-23.
21. R. F. Butler, *J. Geophys. Res.* **78**, 6868 (1973); B. M. Moskowitz, *Earth Planet. Sci. Lett.* **47**, 285 (1980).
22. K. Haneda and H. Kojima, *J. Phys.* **40**, Colloq. C2, Suppl. 3, 583 (1979).
23. Y. Imaoka, Y. Hoshino, M. Sato, in *Ferrites* (University Park Press, Baltimore, 1970), p. 467.
24. D. J. Dunlop, *Geophys. J.* **74**, 667 (1983).
25. C. W. F. Everitt, *Philos. Mag.* **6**, 713 (1961); D. J. Dunlop and G. F. West, *Rev. Geophys.* **7**, 709 (1969).
26. D. J. Dunlop, *Rev. Geophys. Space Phys.* **11**, 855 (1973); D. J. Dunlop and J. M. Stirling, *Geophys. Res. Lett.* **4**, 163 (1977).
27. B. Gustard and W. J. Schuele, *J. Appl. Phys.* **37**, 1168 (1966); I. G. Hedley, *Phys. Earth Planet. Inter.* **1**, 103 (1968); H. Porath, *J. Geophys. Res.* **73**, 5959 (1968).
28. D. J. Dunlop, *J. Geophys.* **40**, 439 (1974); H. H. Thomas, *J. Geophys. Res.* **92**, 11609 (1987); J. Arkani-Hamed, *Geophys. Res. Lett.* **15**, 48 (1988).
29. K. L. Buchan, G. W. Berger, M. O. McWilliams, D. York, D. J. Dunlop, *J. Geomagn. Geoelectr.* **29**, 401 (1977); E. Irving and D. F. Strong, *J. Geophys. Res.* **90**, 1949 (1985); D. V. Kent and N. D. Opdyke, *ibid.*, p. 5371.
30. We thank A. McLean and M. Ward of the Department of Metallurgy and Materials Science for reducing our starting magnetites, M. Back of the Royal Ontario Museum for the x-ray analyses, and B. Head for encapsulating the VRM samples under vacuum. The project was supported by Energy, Mines, and Resources Canada research agreements and by Natural Sciences and Engineering Research Council of Canada operating grant A7709.

12 October 1988; accepted 22 December 1988

Epitaxial Growth of Diamond Films on Si(111) at Room Temperature by Mass-Selected Low-Energy C⁺ Beams

J. L. ROBERTSON, S. C. MOSS, Y. LIFSHTIZ,* S. R. KASI, J. W. RABALAIS, G. D. LEMPERT, E. RAPOPORT

Diamond films (~0.7 micrometer thick) have been epitaxially grown on Si(111) substrates at room temperature with mass-selected 120-electronvolt C⁺ ions. The diamond reflections observed in x-ray diffraction are well localized at their predicted positions, indicating that (i) the diamond(111) and (220) planes are parallel to the Si(111) and (220), respectively; (ii) the diamond rotational spread around its (111) normal is ~1.7°; and (iii) the mosaic block size is ~150 Å. The film growth is discussed in terms of subplantation—a shallow subsurface implantation model. This discovery is an important step toward diamond semiconductor devices.

AMONG THE UNIQUE PHYSICAL properties of diamond that suggest great technological promise are its wide band gap (negligible electrical conductivity) together with its high thermal conductivity (1–4). Diamond synthesis, which remains a challenge, has been achieved in the past 30 years by two main approaches: high pressure–high temperature synthesis (1) of bulk material and low pressure–medium temperature (~600° to 1000°C) synthesis (5–6) of thin films by chemical vapor deposition (CVD). Semiconducting diamond, an attractive material for integrated circuits, has been grown homoepitaxially on diamond substrates (2–4) and polycrystalline diamond films have been grown on many

substrates. This has been established by several methods, including x-ray diffraction that exhibits polycrystalline cubic diamond pattern (6). Recent reviews of this field are now available (2, 6–8). Heteroepitaxial growth of diamond films on non-diamond substrates, a necessity for most electronic device applications, has not yet been reported. We provide here experimental x-ray data that demonstrates heteroepitaxial growth of a diamond film, by means of mass-selected carbon ion beam deposition, on the (111) surface of silicon at room temperature. Diamondlike films have been deposited from carbon ion beams on substrates by different groups (9–11). X-ray diffraction and transmission electron microscopy indicated polycrystalline (diamond) constituents with a grain size of ~100 Å coupled with some larger crystals. Preferred (111) orientation was also noted.

Recently some of us reported (12–14) on thin (~100 to 500 Å) diamond films grown by impinging low-energy (60 to 180 eV) mass-selected C⁺ ions on room-temperature substrates in an ultrahigh vacuum. In situ

surface analysis of the film growth by several techniques at the University of Houston showed the evolution of diamond sp³ short-range order through carbidic and graphitic stages. At higher (200 to 300 eV) or lower (~10 to 30 eV) energies, much higher fluences were needed for the formation of the graphitic phase while the pure diamond sp³ phase was not detected for practical fluences. Following this, thicker films (~1 μm) were deposited on Si(111) crystals at Soreq Nuclear Research Center with the optimal procedure determined in Houston, that is, 120-eV C⁺ ions and a room-temperature substrate. The Si wafers were cleaned prior to the deposition with diluted HF to remove the oxide layer. The current density was ~400 μA/cm² and several hours were required for deposition. The films had a varying thickness profile, corresponding to the beam profile, and thus exhibited color fringes indicating transparency in the visible range (see Fig. 1) which argues persuasively against their being graphitic.

X-ray experiments were confined to the thicker portion of the ~0.7-μm film on Si(111) shown in the photo in order to determine the crystal phase, mosaic character, orientation, and epitaxy. Because the scattering from a 0.7-μm carbon film may be weak, it is difficult to find the carbon peaks in a casual survey alignment scan. The approach adopted here was to align on



Fig. 1. Diamond(111) film epitaxially grown on room temperature Si(111) from 120-eV mass-selected C⁺ ion beam. The color interference fringes are the result of the varying thickness profile of the film. The maximum thickness is on the side where the fringes converge; the number of fringes indicate a thickness of ~7000 Å in that region.

J. L. Robertson, S. C. Moss, Department of Physics, University of Houston, Houston, Texas 77204-5504. Y. Lifshitz, S. R. Kasi, J. W. Rabalais, Department of Chemistry, University of Houston, Houston, Texas 77204-5641.

G. D. Lempert and E. Rapoport, Soreq Nuclear Research Center, Yavne 70600, Israel.

*On sabbatical leave from Soreq Nuclear Research Center, Yavne 70600, Israel.

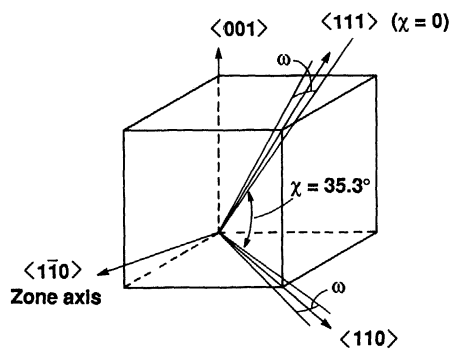


Fig. 2. Scan geometry for the cubic crystal.

reflections from the Si substrate and then to search for corresponding diamond reflections [well documented for crystalline diamond (6, 15)] that would be epitaxially related. The Si(111) surface was oriented with the $\langle 1\bar{1}0 \rangle$ zone aligned on a small goniometer head so as to permit the $\langle 110 \rangle$, $\langle 111 \rangle$, and $\langle 001 \rangle$ directions to be scanned along the conventional (vertical) χ circle of an automated four-circle x-ray diffractometer (Fig. 2). This preliminary alignment was accomplished with Laue photographs that showed sharp undistorted spots from the Si substrate. The goniometer was then transferred to the four-circle instrument on which the angles $\theta(\omega)$ and 2θ are in the horizontal plane, χ is, as noted, on a vertical circle (Fig. 2), and ϕ is a rotation approximately about a $\text{Si}(\bar{1}\bar{1}2)$ direction in the surface. It was our intention to maintain approximately equal angles of incidence and scattering with the (111) surface of the Si crystal while measuring reflections of the form (hkl) such as (111) and (220) in the $\langle 1\bar{1}0 \rangle$ zone of Fig. 2.

The scans θ - 2θ , χ , and ω were performed on the Si reflections for purposes of alignment and instrumental correction; they were then run on the proposed diamond reflections. These scans also indicate the perfection of the crystal: θ - 2θ yields an effective correlation range or particle size; χ and ω scans indicate mosaic spreads. At (111) ($\chi = 0$), for example, the spread in angular distribution of $\langle 111 \rangle$ normals is probed; at other values of χ one may also retrieve information about mosaic block rotation around the surface normal. The distinction between a random polycrystalline film, a highly oriented polycrystalline film [for example, all grains parallel to (111) but randomly oriented around a $\langle 111 \rangle$ direction], and a single crystal epitaxial film may thereby be directly made.

Using graphite-monochromated $\text{Cu-K}\alpha$ radiation from a sealed tube power supply, we located the Si(111) reflection, as indicated above. The diamond(111) reflection was then slowly scanned in θ - 2θ and the result is

shown in Fig. 3a. Next a χ -scan at the θ - 2θ peak position was made; the profile in Fig. 3b shows it to be located at $\sim 1.3^\circ$ (that is, the crystal was reasonably well oriented). Finally, an ω -scan was run with the detector fixed at $2\theta_{\text{Bragg}}$ for diamond(111) as shown in Fig. 3c. This scan required 16 hours. Included in Fig. 3c is the ω -scan at Si(111). If we assume a Gaussian profile for the two peaks, the corrected angular spread of the normals to the reflecting plane (for instance, the diamond $\langle 111 \rangle$ normals) is $\sim 0.5^\circ$ which is a rather narrow mosaic distribution. From a similarly corrected radial θ - 2θ width, the effective correlation range for the diamond mosaic block is $\sim 150 \text{ \AA}$ in the $\langle 111 \rangle$ direction. This short correlation range could be associated with strain as well as particle size. The clear location of a peak in Fig. 3 a, b, and c, confirms it as a proper Bragg reflection.

Rotating χ by $\sim 35.3^\circ$, the Si(220) reflection was next located and precisely aligned.

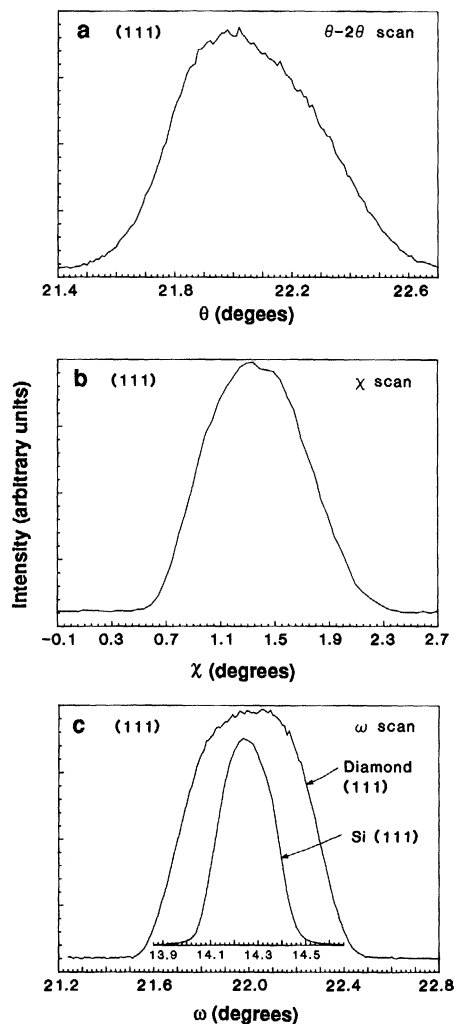


Fig. 3. X-ray profiles for the (111) diamond reflection. (a) θ - 2θ is a radial scan while (b) χ and (c) ω are as in Fig. 2. The Si ω -scan is used as an instrumental correction. The ω angle is identical to θ in an ω -scan but 2θ is fixed.

In a fashion similar to the (111) scans, the predicted diamond(220) reflection was scanned over ~ 31 hours to give the θ - 2θ profile in Fig. 4a. Its effective correlation range is also $\sim 150 \text{ \AA}$, indicating a rather isotropic mosaic block size. A shorter χ -scan in Fig. 4b located this peak at $\sim 36.4^\circ$. The difference, $36.4^\circ - 1.3^\circ = 35.1^\circ$, in turn differs from the exact 35.3° between $\langle 111 \rangle$ and $\langle 110 \rangle$ cubic directions only because the alignment was not precisely in the $\langle 1\bar{1}0 \rangle$ zone and required a small ϕ adjustment. It rules out the possibility of hexagonal diamond(110) ($\Delta\chi = 90^\circ$) or graphite(110) ($\Delta\chi = 80.2^\circ$). The location of both of the cubic diamond reflections on their respective reciprocal lattice points, separated by the correct rotation angle χ , provides convincing evidence for the epitaxial growth of diamond(111) on Si(111), that is $\langle 111 \rangle_{\text{diamond}}$ is parallel to $\langle 111 \rangle_{\text{Si}}$ and $\langle 220 \rangle_{\text{diamond}}$ is parallel to $\langle 220 \rangle_{\text{Si}}$. By epitaxial we mean simply the inheritance of a common orientation (16). It would, of course, be impossible for the lattice spacing of Si to be assumed by diamond in a coherent manner. The interface is thus incoherent but is thereby no less epitaxial.

The intensity in the region of the graphite(002) reflection ($d_{002} = 3.35 \text{ \AA}$) was also explored, assuming that (001) of graphite would be parallel to (111) of Si. In an extended scan, no graphite peak was observed. Table 1 summarizes the data that is relevant for the identification of the cubic diamond phase, ruling out the possibilities of graphite and hexagonal diamond.

Figure 4, c and d presents the ω -scan at (220) and its conversion, by a geometrical argument, to the angular distribution of diamond mosaic blocks around the $\langle 111 \rangle$ axis. At (111) the ω -scan gives the angular distribution of $\langle 111 \rangle$ axes in a cone about the surface normal. At (220) the ω -scan can be used to calculate the degree to which the diamond crystal film tends toward a highly oriented polycrystal. The spread in angular distribution, α , of $\sim 1.7^\circ$ at 1/2 height in Fig. 4d can thus be read as a small spread in the rotation of the mosaic blocks around their common $\langle 111 \rangle$ axis.

These results do not address the question of the volume fraction of epitaxial diamond. It is possible that the crystalline film coexists with a much more disordered material [with nevertheless a (diamond) sp^3 short range order as was detected by several surface analysis techniques (12-14)]. It would not be feasible, however, with the current laboratory x-ray source, to measure such a diffuse amorphous component because its total intensity, which is comparable to the weak diamond reflections, would be radially spread and azimuthally extended over a 360°

Table 1. Comparison of selected crystallographic parameters for cubic diamond, hexagonal diamond, and graphite. The measured $\Delta\chi$ is not exactly 35.3° solely because of a slight misorientation. The d values of the carbon allotropes are American Society for Testing and Materials (ASTM) values (15). The $\Delta\chi$ is calculated for the specific crystal geometry. The values for the deposited film are experimental values.

Phase	2 θ scan			χ scan
	<i>hkl</i>	2 θ	<i>d</i> (Å)	$\Delta\chi$
Cubic diamond	111	43.9°	2.06(ASTM)	35.3° (calculated)
	220	75.3°	1.26(ASTM)	
Hexagonal diamond	002	43.9°	2.06(ASTM)	90° (calculated)
	110	75.3°	1.26(ASTM)	
Graphite	101	44.6°	2.03(ASTM)	80.2°(calculated)
	110	77.5°	1.23(ASTM)	
Deposited film		44.0°	2.06	(35.1°) (experimental)
		75.2°	1.26	

ring. It has previously been shown (17–19) that diamond films grow epitaxially on a diamond host from low and medium energy carbon deposition, especially on the (111) facet (19). Once our diamond(111) film is formed on Si(111), we assume that it continues to grow epitaxially under the carbon fluence; this is in agreement with the observation of a preferred (111) diamond orientation in previous carbon beam deposition work (9–11). It is therefore reasonable to assume that the transparent film reported herein is essentially a diamond mosaic crystal.

The present conclusions can be summarized as follows: (i) The cubic diamond constituent studied here is epitaxially grown on Si(111), namely the (111) diamond plane is parallel to the Si(111) plane and diamond (220) is parallel to Si(220). (ii) The mosaic block size in this diamond constituent is at least 150 Å. (iii) The angular distribution of the mosaic blocks around the $\langle 111 \rangle$ normal is $\sim 1.7^\circ$; the spread in normals is $\sim 0.5^\circ$.

Our results are consistent with a recently proposed model for epitaxial growth by hyperthermal ions (20) which involves shal-

low implantation (suggested name—subplantation) rather than a surface process typical for thermal evaporation or CVD. The subsurface carbon concentration in the host matrix increases with C^+ fluence to form carbon inclusions, while the surface substrate atoms are sputtered and diluted by ion mixing processes until a pure carbon film is formed. The diamond evolution at the optimal energy range of ~ 60 to 180 eV is caused by both the preferential displacement of graphitic bonded carbon atoms, leaving diamond-bonded atoms in their more rigid positions (the displacement energies are 25 eV for graphite and 80 eV for diamond), and to constraints imposed by the existing host matrix. This proposed internal epitaxial growth in the subsurface matrix should be distinguished from conventional epitaxial growth on surfaces (for example, the expected sensitivity to surface impurities is low due to the subsurface internal growth mechanism).

The epitaxial growth of diamond on Si(111) at room temperature is an example of the potential of hyperthermal beams for producing materials with unique properties. Epitaxial growth of several other materials (Ge, Si, GaAs, InP, Ag, and Al) by impingement of hyperthermal species has recently been reported (21–25). The specific case of diamond on Si(111) is, however, an important step towards diamond semiconductor devices.

REFERENCES AND NOTES

1. J. E. Field, Ed., *The Properties of Diamond* (Academic Press, London, 1979).
2. J. C. Angus and C. C. Hayman, *Science* **241**, 913 (1988).
3. M. W. Geis, N. N. Efremov, D. O. Rathman, *J. Vac. Sci. Technol. A* **6**, 1953 (1988).
4. V. K. Bazhenov, I. M. Vikulin, A. G. Guntar, *Sov. Phys. Semicond.* **19**, 829 (1985).
5. B. V. Derjaguin and D. B. Fedosev, *Sci. Am.* **233**, 102 (May 1975).
6. K. Kobashi, K. Nishimura, Y. Kawate, T. Horiuchi, *Phys. Rev. B* **38**, 4067 (1988).
7. R. Meissner et al., *Thin Solid Films* **153**, 1 (1987).
8. H. C. Tsai and D. B. Bogy, *J. Vac. Sci. Technol. A* **5**, 3287 (1987).
9. S. Aisenberg and R. Chabot, *J. Appl. Phys.* **42**, 2953 (1971).
10. E. G. Spencer, P. H. Schmidt, D. C. Joy, F. J. Sansalone, *Appl. Phys. Lett.* **29**, 118 (1976).
11. E. F. Chaikovskii, V. M. Puzikov, A. V. Semenov, *Sov. Phys. Crystallogr.* **26**, 122 (1981).
12. J. W. Rabalais and S. R. Kasi, *Science* **239**, 623 (1988).
13. S. R. Kasi, H. Kang, J. W. Rabalais, *J. Chem. Phys.* **88**, 5914 (1988).
14. S. R. Kasi, Y. Lifshitz, J. W. Rabalais, G. D. Lempert, *Angewandte Chemie (Adv. Mater. Sect.)* **100**, 1245 (1988).
15. See cubic diamond (file 6-675), hexagonal diamond (file 19-268), and graphite (file 23-64) data, in *American Society for Testing and Materials, Powder Diffraction File, Inorganic Phases* (International Center for Diffraction Data, Swarthmore, PA, 1988).
16. D. W. Pashley, in *Layered Structures, Epitaxy, and Interfaces*, *Mater. Res. Soc. Proc.*, J. M. Gibson and L. R. Dawson, Eds. (Materials Research Society, Pittsburgh, 1985), vol. 37, p. 67.

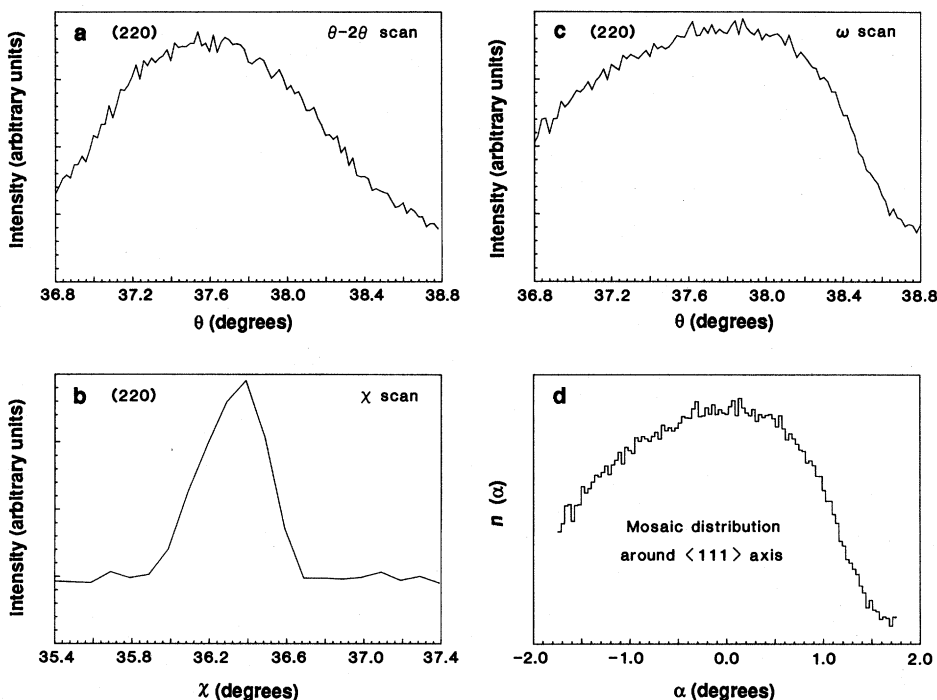


Fig. 4. X-ray profiles (a, b, and c) for the diamond(220) reflection; (d) is derived from (c) where α represents the angular deviation [for example, of a diamond $\langle 111 \rangle$ direction from Si $\langle 110 \rangle$ in the (111) plane] and $n(\alpha)$ is the measured distribution of this deviation.

17. J. H. Freeman, W. Temple, G. A. Gard, *Vacuum* **34**, 305 (1984).
18. R. S. Nelson, J. A. Hudson, D. J. Mazey, R. C. Piller, *Proc. R. Soc. London Ser. A* **386**, 211 (1983).
19. T. E. Derry and J. P. F. Sellschop, *Nucl. Inst. Methods* **191**, 623 (1981).
20. Y. Lifshitz, S. R. Kasi, J. W. Rabalais, *Phys. Rev. Lett.*, in press.
21. K. Miyake and T. Tokuyama, *Thin Solid Films* **92**, 123 (1982).
22. P. C. Zalm and L. J. Beckers, *Appl. Phys. Lett.* **41**, 167 (1982).
23. J. E. Greene *et al.*, *J. Crystal Growth* **79**, 19 (1986).
24. Y. Morishita, S. Maruno, T. Isu, Y. Nomura, H. Ogata, *ibid.* **88**, 215 (1988).
25. S. M. Rossnagel and J. J. Cuomo, *Vacuum* **38**, 73 (1988).
26. This material is based on work supported by the National Science Foundation on grant DMR-8610597, the Department of Energy on grant DE-FG06-87ER45325, and the state of Texas under the (1988-1989) Advanced Research Program. The authors acknowledge the cooperation of Ch. Gilath and M. Kanter from Soreq Nuclear Research Center, Israel.

2 November 1988; accepted 30 December 1988

Atomic Resolution Imaging of Adsorbates on Metal Surfaces in Air: Iodine Adsorption on Pt(111)

BRUCE C. SCHARDT,* SHUEH-LIN YAU, FRANK RINALDI

The adsorption of iodine on platinum single crystals was studied with the scanning tunneling microscope (STM) to define the limits of resolution that can be obtained while imaging in air and to set a target resolution for STM imaging of metal surfaces immersed in an electrochemical cell. Two iodine adlattice unit cells of slightly different iodine packing density were clearly imaged: $(\sqrt{7} \times \sqrt{7})$ R19.1°-I, surface coverage $\theta_I = 3/7$; and (3×3) -I, $\theta_I = 4/9$. The three iodine atoms in the $(\sqrt{7} \times \sqrt{7})$ unit cell form a regular hexagonal lattice interatomic distance $d_I = 0.424$ nanometer, with two atoms adsorbed in threefold hollow sites and one atom adsorbed at an atop site. The (3×3) unit cell showed two different packing arrangements of the four iodine atoms exit. In one of the (3×3) structures, the iodine atoms pack to form a hexagonal lattice, $d_I = 0.417$ nanometer, with three of the iodine atoms at twofold adsorption sites and one atom at an atop site. Another packing arrangement of iodine into the (3×3) unit cell was imaged in which the iodine atoms are not arranged symmetrically.

THE STM HAS PROVEN A VALUABLE tool under ultrahigh vacuum (UHV) conditions for the atomic resolution imaging of semiconductor, layered semimetal, and metal surfaces (1, 2). The application of the STM as an in situ probe of surface structure in heterogeneous catalytic and electrochemical systems requires that the technique be capable of imaging atomic and molecular adsorbates on metal surfaces at atmospheric pressure or in solution or both. Detailed information about adsorbate-substrate bonding, interadsorbate interactions, surface defects, surface diffusion, surface chemical reactions, and interfacial electron-transfer probabilities are some of the potential benefits of STM imaging.

The advantages of the UHV environment for atomic-scale imaging include the ability to prepare well-defined metal surfaces by a variety of means (3) and to prepare single atom probe tips by field emission (4, 5); however, even with these advantages, there have been only a few examples of atomic-scale imaging of adsorbate-covered metal surfaces in UHV (6, 7). The recent imaging of a carbon monoxide-benzene mixed adlat-

tice on a Rh(111) surface in UHV has regenerated hope that the STM can be used to study atomic and molecular adsorbates (7).

In contrast to the UHV environment, the majority of atomic resolution studies in the air and liquid environments of importance to catalysis and electrochemistry have been limited to the layered semimetals such as graphite (2, 8-10), which can be cleaved in air to form flat, ordered, well-defined surfaces. The only exceptions to this rule are reports describing the imaging in air of a hexagonal Au lattice on Au-coated mica substrate (11) and barrier height images of sulfur on Mo (12). The imaged Au surface was shown to have a substantial uncharacterized carbon contamination. Barrier height images of sulfur on Mo(001) showed a characteristic $p(1 \times 2)$ structure; however, the quality of the images was poor, preventing assignment of the sulfur adsorption sites. Solution studies of metal surfaces have been limited to examination of terrace structures (13, 14).

In order to probe the limits of resolution that the STM can be expected to yield in air and ultimately in solution, we have examined iodine-dosed Pt single crystals. The choice of iodine adsorption on Pt as an initial system to study originates in its his-

torical importance to the electrochemistry of well-defined surfaces (15). We also wanted to determine whether STM imaging in air can provide a more detailed understanding of Pt-I bonding interactions than has been obtained from extensive investigations of this system with LEED (low-energy electron diffraction), AES (Auger electron spectroscopy), SEXAFS (surface-extended x-ray absorption fine structure), and electrochemical measurements.

A brief review of previous surface analytical studies on this same system is desirable. Dosing of Pt(111) with iodine in UHV leads to the formation of two possible unit cells (16, 17), $(\sqrt{3} \times \sqrt{3})$, $\theta_I = 0.33$ (structure 1), and $(\sqrt{7} \times \sqrt{7})$, $\theta_I = 0.43$ (structure 2). Adsorption of iodine from a $10^{-3}M$ KI solution leads to the formation of (3×3) , $\theta_I = 0.44$ unit cell (structure 3) (18). Indirect evidence from electrochemical characterization indicates that it is possible to form both structures 2 and 3 by annealing the surface in a H_2 flame and cooling it in a I_2-N_2 carrier gas stream (19). This latter procedure was developed as a means of preparing well-defined platinum surfaces for further electrochemical studies. Silver underpotential deposition (UPD) on surfaces prepared by this methodology displays the same current versus potential behavior as surfaces prepared in UHV (20). The silver UPD results suggest that the iodine dosing procedure can be used as replacement for the UHV ion bombardment and annealing procedure. All of the STM images we present were obtained on surfaces prepared through this non-UHV methodology (21).

The Pt(111) surface was cleaned and ordered in an atmosphere containing iodine (19, 20) in an apparatus equivalent to that described by Zurawski *et al.* (19). The iodine-dosed surfaces were electrochemically characterized with a Bioanalytical Systems CV-27 and reproduced published cyclic voltammograms of iodine-dosed Pt(111) surfaces (16, 19). The surface was imaged with a Nanoscope II (Digital Instruments, Santa Barbara, California) (22). The crystal was always oriented on the STM such that the rows of Pt atoms would be at angles of -30° , 30° , and 90° relative to the x -axis of the microscope scanner. A consistent and defined orientation of the crystal on the microscope stage greatly aided in image interpretation.

As received from Johnson Matthey, the polished face of the Pt(111) crystal was quite rough (60-nm vertical corrugation in a 200-nm scan range). No terrace structure was observable in the STM images. This result was not surprising, as a newly polished single crystal generally requires several days of ion bombardment and annealing in

Department of Chemistry, Purdue University, West Lafayette, IN 47907.

*To whom correspondence should be addressed.